Solar Physics (2022) 297:87
https://doi.org/10.1007/s11207-022-02014-4

Properties of *EUV Imaging Spectrometer* (EIS) Slot Observations

Peter R. Young[1,2] · **Ignacio Ugarte-Urra**[3]

Received: 8 March 2022 / Accepted: 23 May 2022 / Published online: 7 July 2022

Abstract
The *Extreme ultraviolet Imaging Spectrometer* (EIS) on board the *Hinode* spacecraft has been operating since 2006, returning high-resolution data in the 170 – 212 and 246 – 292 Å wavelength regions. EIS has four slit options, with the narrow 1″ and 2″ slits used for spectroscopy and the wide 40″ and 266″ slits used for monochromatic imaging. In this article several properties of the 40″ slit (or slot) are measured using the Fe XII 195.12 Å line, which is formed at 1.5 MK. The projected width of the slot on the detector shows a small variation along the slit with an average value of 40.949″. The slot image is tilted on the detector and a quadratic formula is provided to describe the tilt. The tilt corresponds to four pixels on the detector and the slot centroid is offset mostly to the right (longer wavelengths) of the 1″ slit by up to four pixels. Measurement of the intensity decrease at the edge of the slot leads to an estimate of the spatial resolution of the images in the x-direction. The resolution varies quadratically along the slot, with a minimum value of 2.9″ close to the detector center. Intensities measured from the slot images are found to be on average 14% higher than those measured from the 1″ slit at the same spatial location. Background subtraction is necessary to derive accurate intensities in quiet-Sun and coronal-hole regions. Prescriptions for deriving accurate slot intensities for different types of slot datasets are presented.

Keywords Corona · Instrumental effects · Spectral line · Intensity and diagnostics · Spectrum · Ultraviolet

1. Introduction

The imaging slit spectrometer has been an important tool for studying the solar atmosphere at ultraviolet wavelengths, with routine observations beginning with the *Coronal*

✉ P.R. Young
peter.r.young@nasa.gov

1 NASA Goddard Space Flight Center, Solar Physics Laboratory, Heliophysics Science Division, Greenbelt, MD 20771, USA

2 Department of Mathematics, Physics and Electrical Engineering, Northumbria University, Newcastle upon Tyne, UK

3 Naval Research Laboratory, Space Science Division, Washington, DC 20375, USA

Diagnostic Spectrometer (Harrison et al., 1995), the *Solar Ultraviolet Measurements of Emitted Radiation* (Wilhelm et al., 1995), and the *Ultraviolet Coronagraph Spectrometer* (Kohl et al., 1995), all launched on the *Solar and Heliospheric Observatory* in 1995. The standard mode of operation of these instruments is to image the Sun through a narrow slit with a width of size close to the spectral resolving element of the instrument. The resulting image on the detector shows a set of parallel lines whose positions are the wavelengths of the atomic transitions in the spectrum. The variation of intensity along a line is due to the varying emission of solar features along the slit direction. Images of the Sun can be obtained by scanning the solar image across the slit, which builds up a two-dimensional image exposure-by-exposure in a procedure called "rastering". This can be a time-consuming process and a scan of an active region may take tens of minutes.

High-cadence extreme ultraviolet (EUV) imaging from first the *EUV Imaging Telescope* (Delaboudinière et al., 1995), and more recently the *Atmospheric Imaging Assembly* (AIA: Lemen et al., 2012), have shown that the EUV corona can be highly dynamic. For example, Chitta, Peter, and Young (2021) studied EUV bursts in quiet Sun and a coronal hole and found lifetimes down to the resolution of AIA (24 s). It is thus clear that a single raster image from a spectrometer cannot capture such evolution, yet the plasma diagnostics obtained from a spectrometer are still desirable for understanding the plasma properties.

A compromise solution comes from taking spectroscopic measurements with a wide slit, often referred to as a slot. The detector image will then, in place of the spectral lines, display two-dimensional images at the locations of each of the atomic transitions. By repeated exposures at a spatial location, high-cadence image data can be obtained with the spectrometer. Alternatively, rasters can be performed for larger spatial regions and an image of an entire active region can be obtained in minutes. The disadvantage of slot mode is that the density of atomic transitions in the ultraviolet spectrum is high and so images in nearby lines will overlap, complicating the analysis. Strong, relatively isolated lines can be used with confidence, however. Image ratios of density- or temperature-sensitive diagnostic atomic transitions can potentially be used to yield high-cadence plasma parameters not possible with EUV imagers.

The present article discusses properties of the 40″ slot that is a component of the *EUV Imaging Spectrometer* (EIS: Culhane et al., 2007a) on the *Hinode* spacecraft. It complements the 1″ and 2″ slits that are used for spectroscopy. *Hinode* was launched in 2006 and the first use of slot data for science analysis was by Culhane et al. (2007b), who analyzed three-step rasters with a cadence of 3 min to measure the properties of a coronal-hole jet in a wide range of emission lines.

A novel application of slot data was performed by Innes et al. (2008), who searched for emission that extended beyond the left and right edges of the slot. Such emission is caused by large Doppler shifts of features at the edges of the slot. Velocities of more than 100 km s^{-1} were found in lines such as He II λ256.32 and Fe XV λ284.16.

Ugarte-Urra, Warren, and Brooks (2009) used slot rasters to study the heating and cooling of active-region loops over the temperature range 0.4 to 2.5 MK at a cadence of 70 s. Further loop studies were performed by Ugarte-Urra and Warren (2011) and Warren et al. (2011) who used slot rasters to study the dynamics of active-region outflow regions and fan loops, particularly focusing on Si VII λ275.36 and Fe XII λ195.12, formed at 0.6 MK and 1.5 MK, respectively. Si VII showed apparent inflows in the fan loops in the slot movies, while Fe XII showed apparent outflows; both types of motion were confirmed through narrow-slit Doppler maps from the same regions.

Time-series observations with the slot have been used to study waves and oscillations in various types of solar structure. Banerjee et al. (2009) identified slow magnetosonic waves above the limb in coronal holes using Fe XII λ195.12, with periods in the range 10 to 30 min

and propagation speeds around 125 km s^{-1}. Oscillations in λ195.12 were also reported by O'Shea and Doyle (2009) from an active-region slot dataset with a high 3.1-s cadence. Another λ195.12 active-region loop dataset, with 20 s cadence, yielded evidence for standing slow acoustic oscillations at the looptop and one footpoint (Srivastava and Dwivedi, 2010b). He II λ256.32, Fe XII λ195.12, and Fe XV λ284.16 slot images from a quiet-Sun bright point were analyzed by Srivastava and Dwivedi (2010a) to identify 5-min oscillations in He II and Fe XII lines, but not Fe XV. The cadence was 32 s.

Kontogiannis et al. (2018) used a sequence of slot images at a fixed location in the quiet Sun to study morphology at different temperatures in relation to the magnetic field, and they identified two jets in the He II λ256.3 line.

Harra et al. (2017, 2020) have demonstrated that the 266″ slot data can be used to measure Doppler shifts and identify the hot Fe XXIV λ255.1 emission (formed at 18 MK) line in flares.

Usage of the EIS slot reduced following the launch of AIA on the *Solar Dynamics Observatory* in 2010 as this instrument continuously images the entire solar disk in seven different EUV wavelengths at 12 s cadence and with a higher spatial resolution than EIS. The AIA data can, however, be compromised by uncertainty over the species that are contributing to the EUV channels' bandpasses (e.g., Brosius and Holman, 2012). Hence, there is still value in high-cadence slot imaging with EIS where, at least for strong, unblended lines, one can expect monochromatic images. In addition, there has been renewed interest in slot or slitless spectrometers (Young, 2021) due to the potential of applying deconvolution codes to resolve the spectral and spatial dimensions and thus recover emission line profiles (Winebarger et al., 2019).

As of October 2021, slot observations comprise 9.2% of all EIS observations in terms of observation duration, with 205 days of accumulated data. Given the relatively low number of papers that use slot data, as described above, this is a large dataset that mostly remains unexplored. The present article determines technical parameters for the EIS slot that will be valuable for scientists who wish to exploit the data. The particular questions addressed are:

i) What is the measured width of the slot?
ii) What is the tilt of the slot on the detector?
iii) What is the spatial resolution of the slot?
iv) Are the intensities measured with the slot compatible with the narrow slits?

Section 2 provides an overview of EIS and the slot data. Section 3 addresses the first three questions listed above, and Section 4 the fourth question. In each case we focus on the strong Fe XII 195.12 Å emission line. Section 5 provides a prescription for deriving intensities from slot data, and Section 6 summarizes the results of the article.

2. Overview of EIS and the Slot Data

EIS is described in Culhane et al. (2007a) and it features a short-wavelength (SW) channel from 170 to 212 Å and a long-wavelength (LW) channel from 246 to 292 Å. Spectral resolution is 3000 – 4000 and the spatial resolution is 3 – 4″. Pixels on the detector correspond to 1″ × 1″. A slit/slot mechanism is placed between the primary mirror and the grating, limiting the image field-of-view that reaches the grating. The mechanism has a paddle-wheel design with four blades, each with its own slit. The slits are identified by their projected widths on the Sun and are in the order 1″, 266″, 2″, and 40″. The two wide slits are usually referred to as slots, and the present work focuses on the 40″ slot, which we will often refer to as simply the slot.

The prelaunch radiometric calibration of EIS was described by Lang et al. (2006), and updates, including time-dependent corrections, were provided by Del Zanna (2013) and Warren, Ugarte-Urra, and Landi (2014). All intensities provided in the present article were derived using the prelaunch calibration. Procedures for converting to the Del Zanna (2013) or Warren, Ugarte-Urra, and Landi (2014) calibrations are described on the EIS Wiki.

EIS has two 2048 × 1024 pixel CCDs, one for each of the two channels, with the long and short dimensions corresponding to wavelength and the slit/slot length, respectively. The latter is aligned with the solar south–north direction. One pixel corresponds to 1.0″ in the x and y dimensions and 22.3 mÅ in the x-direction (solar-x and wavelength dimensions are mixed for slot data). The onboard software restricts downloaded detector images to 512 pixels in the y-direction, so two exposures are required to obtain the complete extent of the EIS slits. Generally EIS observations are cocentered with the *Solar Optical Telescope* on *Hinode*, which results in a y-center located at about y-pixel 592 (80 pixels higher than the CCD center). Thus, the y-pixel region most widely downloaded is 336 to 847. Y-pixels are indexed from 0 to 1023, although the onboard software prevents pixel 0 from being downloaded. The bottom pixel of the observed detector window is referred to as the y initial position (YIP).

The complete EIS wavelength bands are usually not downloaded in order to conserve telemetry. Instead *wavelength windows* are specified, centered on strong or diagnostically important emission lines. The onboard software restricts the window sizes to be multiples of eight pixels. Windows of 40 pixels are the minimum required for slot datasets, but 48 pixels are recommended to enable a background intensity level to be estimated.

Figure 1 shows a slot exposure obtained on 15 May 2007 at 05:41 UT with the EIS study SYNOP001. The complete EIS spectral range is shown over the four plots and 110 pixels along the y-direction (corresponding to 110 arcsec). A 30-s exposure was used. The radiometric calibration has been applied, which results in the Fe IX λ171.06 line appearing quite bright even though the effective area at this location is very weak. Conversely, the strongest line in the EIS spectrum in terms of counts – Fe XII λ195.12 – appears less strong. In the bottom half of the image there is a quiet-Sun bright point that is most prominent in Fe XV λ284.16. The slot images as they appear on the detector are reversed in the x-direction compared to the true solar image. Although the slot is identified as being 40″ wide, it is actually closer to 41″ (Korendyke et al., 2006). Due to the line spread function (LSF) of the instrument, the sharp edges of the slot are blurred in the images and the total extent of a slot image in the dispersion direction is about 46″.

The most prominent regular slot observation is the full-Sun scan performed every three weeks as part of *Hinode* Operation Plan (HOP) 130. The large-format study 480″ × 512″ full_sun_slot_scan_2 (and its earlier version full_sun_slot_scan_1) is run over multiple spacecraft pointings in order to provide image mosaics that cover the entire solar disk in a few hours. These data have been valuable for monitoring the EIS radiometric calibration (Warren, Ugarte-Urra, and Landi, 2014). EIS Fe XII λ195.12 full-disk mosaics are compared with irradiance observations by the *EUV Variability Experiment* (Woods et al., 2012) to establish the EIS absolute calibration and the sensitivity decay over time.

All of the slot images are blended with images from nearby lines to some extent, but the lines listed in Table 1 (and marked on Figure 1) give relatively clean images with a good signal. For each line in Table 1 the wavelength from version 10 of CHIANTI (Young et al., 2016; Del Zanna et al., 2021) is listed. The temperature of maximum emission [$T_{\rm mem}$] (computed with CHIANTI) is the temperature at which a line's contribution function peaks.

Figure 2(a) shows the Fe XII λ195.12 image from the fifth exposure of a raster observation obtained on 31 January 2008 at 22:35 UT. It was obtained above the west limb of

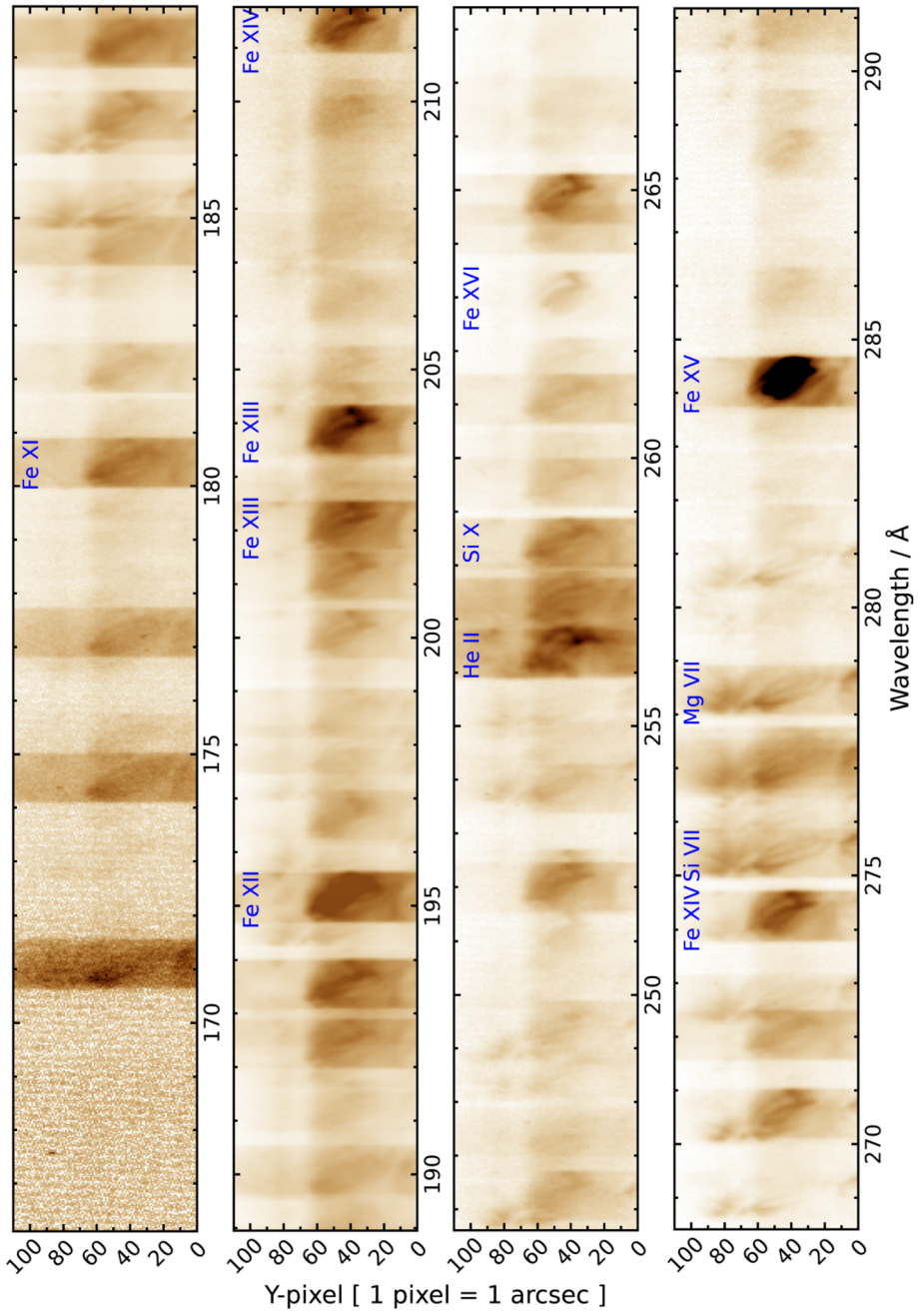

Figure 1 A complete EIS spectrum obtained with the 40″ slot, derived from an observation on 15 May 2007 at 05:41 UT. An inverse, square-root intensity scaling has been applied and an artificial saturation to bring out the weaker features.

Table 1 Slot lines that are mostly unblended.

Ion	Wavelength	Log $T_{\rm mem}$	Ion	Wavelength	Log $T_{\rm mem}$
He II	256.32	4.95	Fe XIII	203.83	6.24
Mg VII	278.40	5.79	Fe XIII	202.04	6.25
Si VII	275.36	5.79	Fe XIV	211.32	6.29
Fe XI	180.40	6.12	Fe XIV	274.20	6.29
Si X	258.37	6.15	Fe XV	284.16	6.34
Fe XII	195.12	6.19	Fe XVI	262.98	6.43

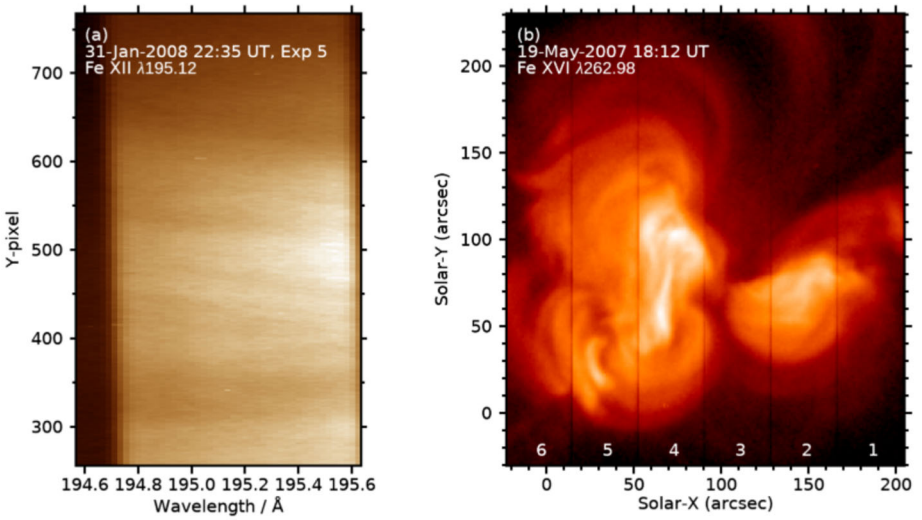

Figure 2 (a) a slot image of the Sun in Fe XII λ195.12 obtained in a quiet region above the west limb on 31 January 2008 at 22:35 UT. (b) a slot-raster image in the Fe XVI λ262.98 line, obtained from an observation on 19 May 2007 at 18:12 UT. The numbers at the bottom indicate the order in which the raster is built from the six exposures. A logarithmic intensity scaling has been applied.

the Sun in quiet conditions and it is displayed in the detector frame, so east and west are reversed. The wavelength window was set to 48 pixels wide by 512 pixels high, and thus there is background emission on the left side, and a little on the right side. The aspect ratio has been modified in order to better illustrate the tilt of the slot image, which can be seen to be about 2 – 3 pixels in the wavelength direction.

By adjusting the primary mirror position, wide-field images of the Sun can be obtained through raster scans and Figure 2(b) shows an example from an active-region observation on 19 May 2007 that used six raster positions. An exposure time of 30 s was used, and the step size between exposures was set to 36″. Thin vertical lines can be seen on the image, revealing the six individual exposures that comprise the total image. As will be shown later, the intensity falls off at the edges of the slot and so, even though the step size is smaller than the slot width, it is not small enough to avoid the intensity drop-offs. To obtain images with a completely smooth intensity distribution, a step size of 32 pixels is recommended, and this is implemented in HOP 130.

The EIS datasets used in this article are freely available from the *Virtual Solar Observatory* (sdac.virtualsolar.org), and the IDL software used for data analysis are available in

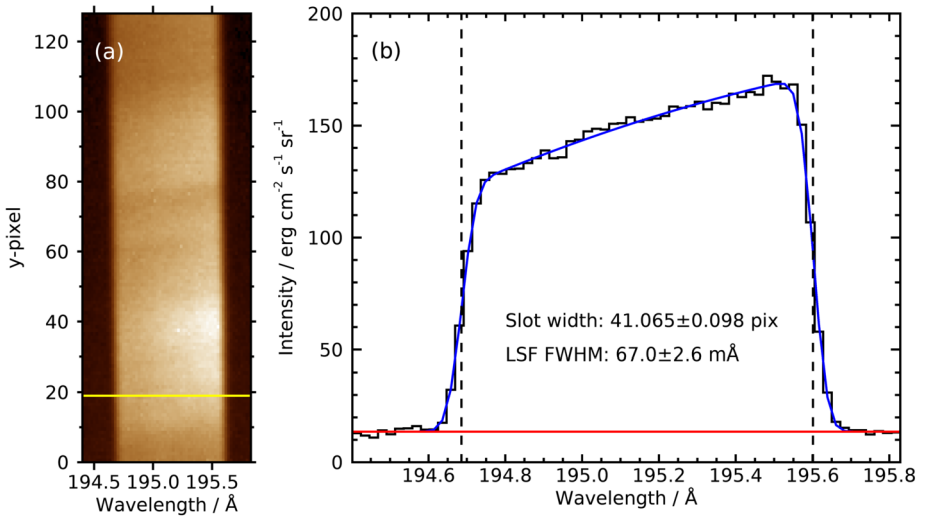

Figure 3 (a) the Fe XII λ195.12 slot image obtained at 13:12 UT on 20 September 2021. (b) the intensity cross section through the slot image at *y*-pixel 19 (indicated by the *yellow line* on Panel a). The *blue line* shows the seven-parameter fit to the intensity, the *horizontal red line* shows the fitted background intensity, and the *vertical dashed lines* show the edges of the slot as derived from the fit.

the *Solarsoft* (sohowww.nascom.nasa.gov/solarsoft) library, except where otherwise noted. IDL software for generating the figures in this article are available in the GitHub repository papers/2022_eis_slot, which also contains derived data products.

3. Slot Tilt, Width, and Spatial Resolution

In this section we address the first three questions identified in the Introduction by applying a fitting function to the intensity distribution across the dispersion direction of slot images. Fe XII λ195.12 is chosen for this analysis as it is normally the strongest line observed by EIS, and thus offers the best opportunity for constraining the slot parameters. The results enable us to determine the variation of slot width and spatial resolution along the full length of the slot, and to measure the tilt of the slot that is apparent in Figure 2(a). The latter then allows us to compare the relative positions of the 1″ and 40″ slits on the detector.

3.1. Fitting Method

The method chosen for estimating the slot tilt and width was to perform a relatively simple parametric fit to the distribution of intensity in the dispersion direction (Figure 3). Fe XII λ195.12 is ordinarily the strongest line observed by EIS and, because the corona emits strongly at the ion's formation temperature of 1.5 MK, there is usually a good signal over the full slot image frame. However, the emission is often highly inhomogeneous, as illustrated in Figure 1, and thus not susceptible to a limited parameter fit.

An exception is quiet-Sun emission above the limb. Above heights of around 50″ there is little contribution from bright points and the emission is relatively uniform with a decreasing intensity with radial distance. There is no option to roll the Hinode spacecraft so the

EIS slot is always oriented north–south. The preferred observation for off-limb quiet-Sun measurements is then for the slot to be centered near the Equator.

Figure 3 shows an example from a dataset obtained on 20 September 2021 that is analyzed in the following section. The data have been binned by 4 pixels in y to improve signal to noise; the original data have 512 y-pixels. The left panel shows the Fe XII λ195.12 slot image, and y-pixel 19 is indicated. The intensity pattern across the slot is shown in the right panel, and a simple, almost linear decrease in intensity across the slot can be seen.

The data for these off-limb datasets were fit as follows. The distribution of intensity shown in Figure 3 was fit with a quadratic function, convolved with a boxcar function, and then convolved with a Gaussian. The boxcar is used to model the sharp edges of the slot, and the Gaussian simulates the line spread function of the instrument. The function is then added to a constant background. There are seven free parameters in this function: three parameters for the quadratic function, one for the left edge of the slot, one for the slot width, one for the width of the Gaussian, and one for the background. The IDL routine eis_fit_slot_exposure was written to perform the fits and is available in a GitHub repository (github.com/pryoung/eis_slot), where further details are given in a README file. The routine calls the MPFIT IDL procedures (purl.com/net/mpfit) (Markwardt, 2009) to obtain the best fit to the intensity profile through χ^2 fitting. The fit for the intensity profile in Figure 3 is overplotted as a *blue line*, and the derived slot width and the full-width at half-maximum (FWHM) of the LSF are indicated. The LSF FWHM corresponds to 3.0″, which agrees with the value of Ugarte-Urra (2016) that was derived from images of small transition-region brightenings.

3.2. A Full-Slit Observation

As discussed in Section 2, emission from the slot extends over the full height of the detector but individual exposures are restricted to 512 pixels. It is thus necessary to schedule two observations for the bottom and top halves of the detector. The studies must also have a wavelength window of at least 48 pixels for Fe XII λ195.12 to enable an accurate fit to the intensity profile. No such observations were found in the EIS archive and so a special observation was obtained on 20 September 2021.

Quiet Sun above the limb was observed and two pointings were performed for each raster to take the top and bottom halves of the detector. Multiple datasets were taken over an 80-min period beginning at 12:02 UT and we focus here on two rasters obtained with the dei_qs_80_slot40 study and beginning at 13:11:21 UT and 13:12:28 UT. The study performs a 2-step raster with a 40″ step size and a 30-s exposure time. Only the first steps of the two rasters are considered here, and the two exposures are centered at $x = 1080''$, about 120″ above the limb. The first exposure is at YIP=1 and the second at YIP=512.

The data were binned by four pixels in the y-direction in order to improve signal-to-noise and to minimize the effect of missing pixels. The latter are flagged by the EIS calibration software (Young, 2022a) and are mainly due to pixels with anomalously high dark currents (warm and hot pixels). Warm pixels can comprise up to 28% of the detector pixels (Kennedy and Young, 2022), hence binning mitigates their effect. Using the fitting procedure described in the previous section, the λ195.12 emission across the slot was fit with the seven-parameter function. The bottom edge of the slot is apparent in the YIP=1 exposure, such that appreciable signal is only seen for detector y-pixel 7 and above. The top edge of the slot is not apparent in the YIP=512 exposure.

Figure 4 shows the results of the intensity profile fitting for the two datasets. The slot centroid is obtained from the fit parameters by adding half the slot width to the wavelength

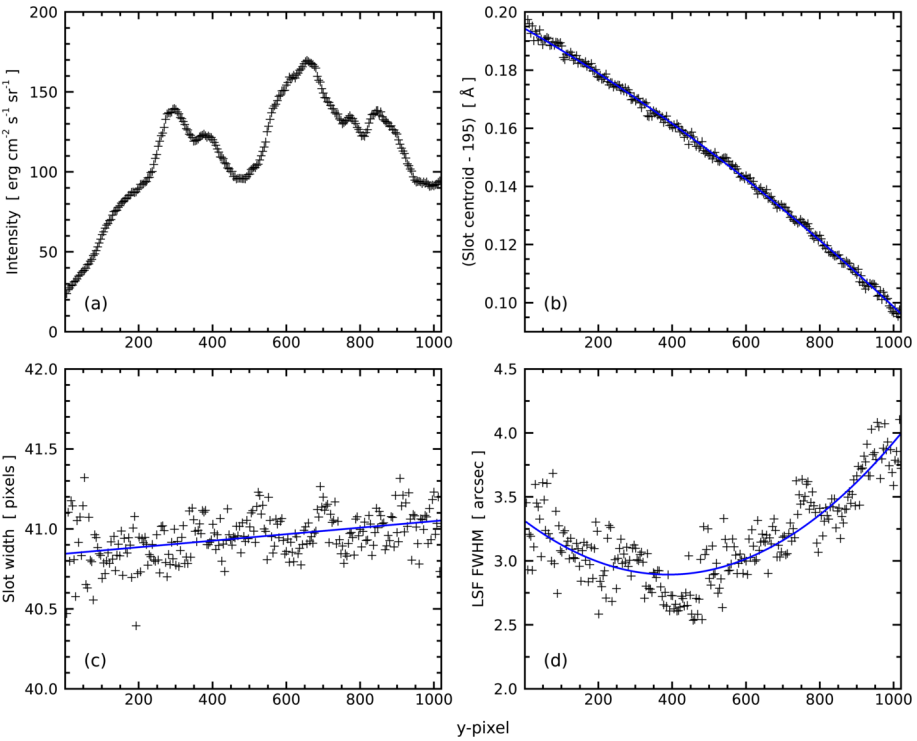

Figure 4 Slot parameters as a function of detector y-pixel for an observation obtained at $x = 1080''$ on 20 September 2021. The parameters are: (a) average intensity across the slot, (b) slot centroid, (c) slot width, and (d) line-spread function FWHM. The *blue curves* on panels (b)–(d) show the polynomial fits to the data.

Table 2 Slot parameters derived from the 20 September 2021 observation.

Quantity	a_0	a_1	a_2
Centroid	–	−7.260(−5)	−2.316(−8)
Width	40.8445	2.038(−4)	–
LSF FWHM	7.384(−2)	−4.818(−5)	6.186(−8)

for the left edge of the slot. The average slot intensity shown in Panel (a) is computed by averaging the 35 pixels centered on the centroid pixel; the full slot width is not used as the intensity falls off near the edge of the slot (Figure 3). The slot centroid is shown in Panel (b), the slot width in Panel (c), and the FWHM of the Gaussian LSF is shown in Panel (d). The latter is plotted in arcsec units, and the conversion factor back to Å is 0.02228. The three quantities were fit with polynomial functions: third-order functions for the centroid and LSF FWHM, and a second-order function for the slot width, which shows a much smaller variation. The fits are shown as *blue curves* on Panels (b) to (d), and the polynomial coefficients are given in Table 2. Thus, the parameter value derived from the fits for a pixel y is given by $\sum_i a_i y^i$. The a_0 value is not given for the slot centroid because the positions of lines on the detector shift during an orbit due to thermal effects (Kamio et al., 2010), and so a_0 is dataset specific.

Table 3 EIS datasets used to measure slot parameters.

Date	Time [UT]	Study	N_λ	YIP
31-Jan-2008	22:37	Slot_raster	48	256
5-Jun-2012	21:06	SI_Venus_slot_v1	48	319
9-May-2016	19:10	SI_Mercury_slot_v1	48	212
13-May-2020	21:06	Alignment_modify_v2	48	294

The LSF FWHM is interpreted here as a measure of the spatial resolution of the slot. The best resolution of 2.9″ occurs at y-pixel 384, and the worst resolution of 4.0″ at the top of the detector (y-pixel 1023). Section 2 mentioned that EIS is usually centered on the SOT field-of-view, corresponding to y-pixel 592, where the resolution is 3.0″. The spatial resolution may show some variation with the primary mirror position, which is not investigated in the present work. The relevant instrument parameter is the fine mirror position, discussed in Section 4.1.

3.3. Time Variation

The tilts of the narrow EIS slits were measured early in the mission and are obtained with the IDL routine eis_slit_tilt. Fourth-order polynomials were fit to the variation of line centroids over the full height of the detector, and the parameters are stored in the file eis_slit_tilt.txt within the EIS Solarsoft directory. An adjustment to the grating-focus mechanism was performed on 24 August 2008 and so different parameters apply before and after this date. We thus expect a similar change for the slot parameters.

As slot data covering the full height of the detector, with a sufficiently wide spectral window, were not available prior to the 20 September 2021 observation described in the previous section, the best that can be done is to compare datasets that obtain the maximum 512 pixels allowed in one exposure.

The EIS archive was searched for slot datasets with 512 pixels along the slot, at least 48-pixel-wide wavelength windows, and a pointing above the limb in quiet-Sun conditions. The spatial locations were checked using the EIS_Mapper software (eismapper.pyoung.org) to determine if the observations avoided active regions. Very few suitable datasets were found over the mission lifetime, but four were selected from different times during the mission and are listed in Table 3. N_λ is the number of wavelength pixels used for λ195.12.

For each of the four datasets, one data file was chosen, and the best exposure within the raster was selected based on signal-to-noise and distance from the limb. Two-pixel binning was applied to each of the four datasets, and the intensity profiles were fit using the eis_fit_slot_exposure routine. The slot centroids were derived from the fits, as described in Section 3.1, and the variations of the centroids along the slit were fit with linear functions. The gradients are listed in the third column of Table 4. Linear functions were used instead of the quadratics used in Section 3.2 because the datasets covered 512 pixels of the detector instead of 1024 pixels.

In order to compare with the full-slot data from Section 3.2, subsets of the full-slot centroid data were extracted to match the pixel ranges of each of the four datasets. Linear functions were then fit to these subsets to yield the tilt gradients given in column 4 of Table 4. The gradients vary because of the different YIP values of the four datasets (fifth column of Table 3).

As expected, there is a large difference between the 2008 dataset and the 2021 dataset, as the former occurred before the grating change on 24 August 2008. The tilt becomes smaller

Table 4 Slot parameters derived from observations.

Date	Exposure[a]	Tilt [μÅ pix^{-1}]		Difference[b]
		Measured	2021	
31-Jan-2008	5/16	-113.0 ± 0.8	-93.7 ± 2.0	−21.9%
5-Jun-2012	4/6	-99.7 ± 0.6	-98.9 ± 2.0	−0.8%
9-May-2016	3/6	-97.5 ± 1.2	-92.0 ± 2.0	−6.0%
13-May-2020	3/3	-102.2 ± 0.5	-96.3 ± 2.0	−6.1%

[a] m/n – the mth exposure of n.

[b] Percentage difference relative to the 2021 dataset.

after this date, and the change is consistent with that found for the narrow slits. The 2012 and 2021 tilts are close, but the 2016 and 2020 datasets show larger tilts (by magnitude) than the 2021 dataset by 6%. This could be due to thermal changes within the instrument.

The tilt is of value in the present work in relation to background subtraction for the slot intensities, and high accuracy is not required. Our recommendation is to use the Table 2 fit parameters for datasets after 24 August 2008, and the 31 January 2008 tilt value from Table 4 before this date.

3.4. Slit and Slot Tilt Comparison

Figure 5 compares the position of the slot centroid on the EIS detector with that of the 1″ slit for the periods before and after the grating change on 24 August 2008. The tilts of the slot are from the analysis of Sections 3.2 and 3.3. The slit tilts come from the IDL routine eis_slit_tilt. To obtain the relative positions of the slit and slot, it is necessary to use two exposures that are close in time, as the projected slit positions on the detector vary during the 98.5-min *Hinode* orbit. For the period before the grating movement, the SYNOP001 dataset beginning at 18:05 UT on 9 May 2007 was used. A patch of relatively uniform emission in the slot image was identified and the 7-parameter slot fit function was applied to yield the centroid. The same spatial region in the slit exposure was averaged and fit with a Gaussian to yield the slit centroid. The difference fixes the relative offset between the slot and slit. Further details on this process can be found in the code used to generate Figure 5, available in the GitHub repository papers/2022_eis_slot.

The 20 September 2021 dataset (Section 3.2) was used to derive the slot–slit offset for the period after the grating move. The dei_qs_80_slot40 exposure at 13:12:28 UT (used in Section 3.2) was followed by a slit exposure from the study SK_DEEP_5x512_SLIT1 at 13:14:50 UT. The latter study was run specifically to obtain an exposure at the same fine mirror position (see Section 4.1) as the preceding slot study and for the same detector y pixels. To match the processing of the slot data, the narrow-slit data were binned in the y-direction by four pixels, and λ195.12 was fit with a Gaussian along the slit direction to yield the line centroids. The centroids were averaged over positions 48 to 52, and compared with the slot centroid at the same position to yield the relative offset of the slot to the slit.

Figure 5 shows that the tilt is significantly greater for the slot, varying by more than four pixels over the detector height, compared to one pixel for the narrow slit. The curves intersect at y pixels 766 and 737 for the periods before and after the grating move, respectively. Thus, a slot exposure is mostly offset to the right of a slit exposure on the detector. This is significant because the EIS planning software positions the slot wavelength windows assuming the centroid is the same as the 1″ slit. This is why slot exposures such as the one shown in Figure 2(a) are usually offset to the right of the wavelength window.

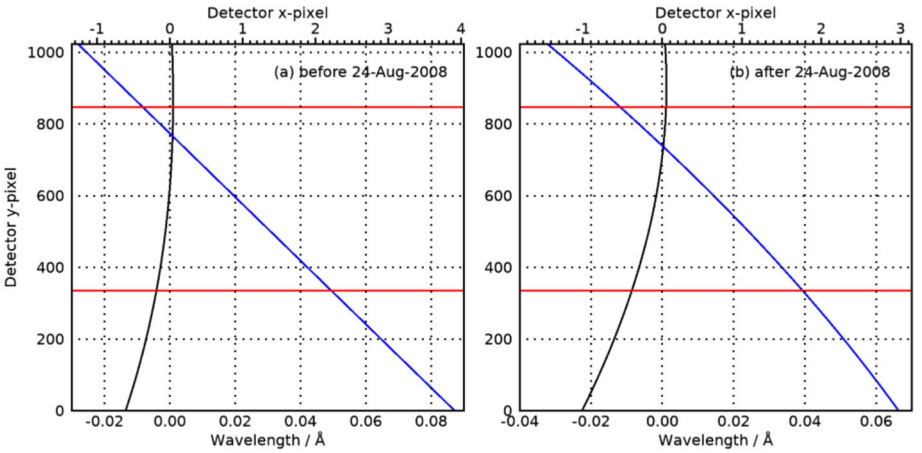

Figure 5 Comparisons of the 1″ slit (*black*) and the centroid of the 40″ slit (*blue*) as they appear on the EIS detectors. Panels (a) and (b) show the positions prior to and after the grating movement on 24 August 2008, respectively. The *red horizontal lines* indicate the portion of the detector that is most actively used.

4. Slit–Slot Intensity Comparison

In this section we present the procedure for comparing Fe XII λ195.12 slot image intensities with intensities derived from the 1″ slit. Intensities are compared for a set of datasets obtained in May 2007, and a correction factor to be applied to slot data is suggested.

4.1. Slit/Slot Alignment

EIS performs raster scans through fine-scale motions of the primary mirror. For a fixed mirror position, if the slit/slot mechanism is rotated from the 1″ slit to the 40″ slot, then the slit is approximately centered within the slot image. The user can check the fine mirror position [FMIRR] with the following IDL command

```
IDL> fmirr=*(d->getaux_data()).fmirr
```

where d is an EIS data object. For a raster observation there will be an FMIRR value for each step of the raster. A single step corresponds to about 0.25″ but the EIS onboard software restricts mirror steps to 1″ or 4 steps. The EIS raster direction is always solar-west to solar-east, or right-to-left in displayed raster images. The raster direction corresponds to increasing FMIRR values. An FMIRR value around 1870 corresponds to the center of the SOT field-of-view. The datasets from 20 September 2021 used in Section 3.2 had an FMIRR value of 1361, and the SYNOP001 datasets described in Section 4.3 mostly had FMIRR values of 1800.

4.2. Intensity Calibration for Slot Data

The routine eis_prep converts the signal measured by the instrument to calibrated intensity units, and the steps involved are described in Young (2022a). One of the factors in this conversion is the effective-area curve, which shows significant variation with wavelength (the curves can be generated with the IDL routine eis_eff_area). For example, the effective area takes values of 0.074, 0.30, and 0.033 cm^2 at wavelengths of 185, 195, and 205 Å,

respectively. Slot data differs from slit data in that the image in a strong line will dominate on the CCD over an extended wavelength region: 40 pixels in the case of the 40″ slot and 266 pixels in the case of the 266″ slot. Thus, Fe XII λ195.12 extends over 194.7 to 195.6 Å in 40″ slot data. In this case, eis_prep takes the effective-area values at the edges of the wavelength window, averages them, and applies this value to the whole window. This is reasonable for small windows, such as those from the 40″ slot, but not for the 266″ windows. It is also not correct for datasets for which windows are the entire CCD. In the latter case, a single effective area value is applied to all wavelengths. In these cases the solution is to leave the data in DN units by giving the /noabs keyword to eis_prep. The window of interest (within the full CCD) should then be extracted and the calibration factor calculated for the wavelength that gives rise to the dominant emission. The routine eis_slot_calib_factor is available in *Solarsoft* for this purpose. For the present article all Fe XII λ195.12 slot intensities were derived using the effective-area value at 195.12 Å.

4.3. The SYNOP001 Study

In order to compare intensities obtained with the slot to those obtained with the slit, it is necessary to obtain exposures close in time to avoid any changes due to plasma evolution. For the present work, the EIS study SYNOP001 was used.

Hinode is pointed to the disk center every day in order for XRT to obtain full-disk synoptic images. Prior to February 2008 this was done approximately every six hours, but this was changed to every 12 hours following the failure of the X-band antenna and the corresponding reduction in telemetry. The XRT synoptic periods last 10 min and EIS typically performs short-duration studies.

The study SYNOP001 was run during the XRT synoptic periods for the periods 2006 December through February 2008, and then replaced with SYNOP005, which ran until 2011 February. For the period February 2009 to October 2009 SYNOP005 and SYNOP001 were often alternated in the XRT synoptic slots.

SYNOP001 consists of two rasters. The first obtains two exposures of 30 s and 90 s with the slot at the same spatial location, and the second obtains two exposures of 30 s and 90 s with the 1″ slit. The default study setting uses the same FMIRR value for both rasters, which puts the 1″ exposure approximately at the center of the slot image. The 90-s slot exposure often results in detector saturation for Fe XII λ195.12, and is not used here. For the present work only the 30-s exposures are considered. The slot and slit 30-s exposures are separated in time by 2 min and 15 s.

SYNOP005 is a less data-intensive study version of SYNOP001, with just single 90-s exposures for the slot and slit. Also, 14 spectral windows were used rather than obtaining the full CCD.

4.4. Slit/Slot Intensity Comparison from SYNOP001

In this section we process the SYNOP001 datasets from May 2007 in order to compare the Fe XII λ195.12 slot and slit intensities for the same spatial locations on the Sun. As noted above, the slit exposure is obtained 2 min and 15 s after the slot exposure, which limits the effect of time evolution on the intensity comparison.

There were 69 SYNOP001 slit-slot dataset pairs and, for each of these, a Gaussian was fit to the narrow slit λ195.12 profile at each of the 256 pixels along the slit using the IDL routine eis_auto_fit (Young, 2022b). The average centroid of the fits was then matched to the nearest wavelength pixel on the CCD. The same pixel in the slot dataset was identified,

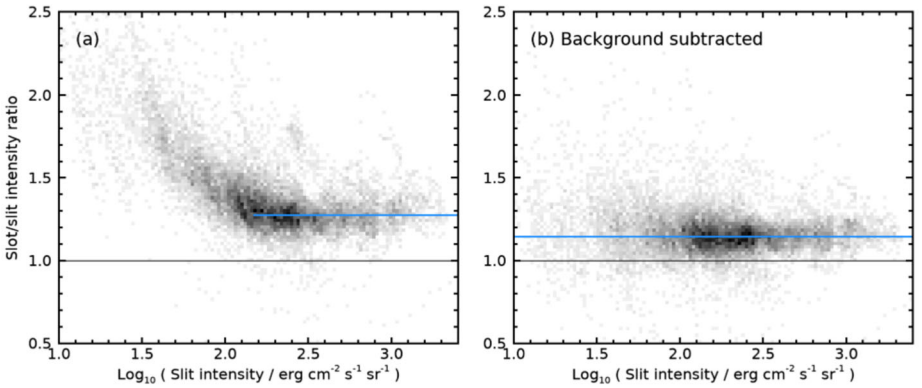

Figure 6 Heatmaps showing ratios of slot to slit intensities for the May 2007 SYNOP001 datasets, plotted as a function of the slit intensity. The bin sizes are 0.02 in both dimensions, and the maximum values are 53 (a) and 56 (b). For display purposes the maps are shown scaled to the power 0.7. Panel (b) shows the effect of background subtraction for the slot intensities. The *blue horizontal line* on Panel (a) shows the mean ratio value for slit intensities ≥ 150 erg cm^{-2} s^{-1} sr^{-1}, and that on Panel (b) shows the mean ratio value for all slit intensities.

and the intensity was averaged for this pixel and its neighbors, to allow for the small tilt of the narrow slit.

The Gaussian fit to the slit data automatically accounts for the background-intensity level in the narrow-slit spectrum. For the slot, the background intensity was computed by first obtaining the centroid pixel of the slot by adjusting the slit centroid for the slot–slit offset (Figure 5). The two pixels ± 28 pixels from the slot centroid were identified and, for each, the five pixels centered on these pixels were averaged, yielding background estimates on the left and right sides of the λ195.12 slot image. These two values were then averaged to give the final background intensity.

Two of the 69 datasets were rejected due to anomalies with the slot image, and four further datasets because either the YIP or FMIRR values did not match between the slit–slot pairs. In addition, all slot intensities larger than 2740 erg cm^{-2} s^{-1} sr^{-1} were rejected as the detector saturates at this level. For all remaining pixels, Figure 6(a) shows the ratios of the slot to slit intensities, while Figure 6(b) shows the ratios after subtracting the slot background. This demonstrates clearly that background subtraction is necessary for slit intensities ≤ 150 erg cm^{-2} s^{-1} sr^{-1}. For intensities larger than this, the ratios without background subtraction are approximately constant and we find an average ratio of 1.27 with a standard deviation of 0.13. For the entire set of background-subtracted data the average ratio is 1.14 with a standard deviation of 0.14, and for intensities ≥ 150 erg cm^{-2} s^{-1} sr^{-1} the average ratio and standard deviation are 1.13 and 0.10. For reference, we note that Brooks et al. (2009) gave an average intensity for λ195.12 in quiet Sun of 135 erg cm^{-2} s^{-1} sr^{-1}.

We do not have an explanation for why the slot intensity is systematically higher than the slit intensity across the SYNOP001 datasets. We do not believe that it is due to blending not accounted for by the background subtraction. For example, we know that about half of the image in the weak Fe VIII 194.66 Å line overlaps with the λ195.12 image. The Fe VIII image will be inhomogeneous, and thus the five-pixel strip used to define the background on this side of the λ195.12 image and that runs through the λ194.66 image will not necessarily represent that part of the λ194.66 image that overlaps with λ195.12. If the background strip is weaker than the overlap region then the derived λ195.12 intensity will end up brighter

due to the unaccounted for Fe VIII component. However, equally, if the background strip is brighter than the overlap region, then the λ195.12 will be lower than expected. Thus, on average, we would expect inhomogeneities in the blending-line images to cancel out rather than lead to an overestimate of the λ195.12 intensity.

Another possibility for the intensity discrepancy is that the 1″ slit width is not correct. In particular, the eis_prep routine assumes that the slit width is exactly 1″. If it is in fact 0.88″ wide then this would account for the discrepancy. That is, a given count rate would convert to an intensity 14% higher than currently computed by eis_prep. As stated earlier, the slit widths were measured prelaunch and Korendyke et al. (2006) gave the measured widths of the 1″ and 40″ slits to be 9.5 ± 0.5 μm and 384 ± 2 μm, respectively. Using the value of 40.949″ for the slot width from Section 3.2 then gives the 1″ slit width to be $1.01'' \pm 0.05''$. Therefore, our measured slit/slot intensity discrepancy lies outside the uncertainties of the laboratory slit measurements.

The λ195.12-line profiles from the SYNOP001 datasets were fit with single Gaussian functions. Generally these fits are good, but Peter (2010) demonstrated that most profiles of Fe XV λ284.16 from an active region show evidence of excess emission in the wings. To investigate this, we computed intensities from all of the SYNOP001 line profiles by summing ±7 pixels either side of the pixel nearest the centroid derived from the Gaussian fit, and subtracting the background level obtained from the Gaussian fit. Comparing these intensities with the Gaussian-derived intensities we found a median excess of 1.7%, which again is insufficient to explain the slit–slot intensity discrepancy. Wing emission beyond 7 pixels can not be accurately assessed due to blending species – see, for example, Figure 6 of Young et al. (2009).

Without an explanation for the enhanced slot intensities, our suggestion is that Fe XII λ195.12 slot intensities should be divided by the *empirical correction factor* of 1.14 in order to reproduce the 1″ slit intensities.

The fact that the nonsubtracted intensity ratio becomes constant for higher intensities implies that the background level in the slot spectrum scales with the Fe XII intensity. This is despite the fact that the emission lines contributing to the background are not due to Fe XII. Our explanation is that, although lines formed at different temperatures vary in different amounts according to solar conditions (coronal hole, quiet Sun, active region), to a first approximation they scale together. Consider the intensity measurements from Table 2 of Brown et al. (2008), in particular the "QS", "AR2", and "Limb" values for the nearby lines of Fe VIII λ194.66, Fe XII λ195.12, and Fe X λ195.40. Normalizing the λ195.12 intensity to 100 in each of the three regions, the intensities for λ194.66 are 10.8, 11.0, and 6.2 for QS, AR2, and Limb, respectively. The intensities for λ195.40 on the same scale are 6.4, 6.9, and 4.0, respectively. That is, to within a factor two, the Fe VIII and Fe X intensities scale with Fe XII for these three regions, even though Fe XII varies by more than a factor 10 across the three regions.

This scaling of the background with Fe XII intensity will prove valuable later in providing a prescription for deriving intensities from slot data (Section 5.2).

5. A Prescription for Measuring Intensities from Slot Data

The results from the present work suggest the following prescription for measuring accurate Fe XII λ195.12 line intensities from EIS slot data when the wavelength windows are at least 48 pixels wide:

i) Calibrate the data to erg cm^{-2} s^{-1} sr^{-1} units.

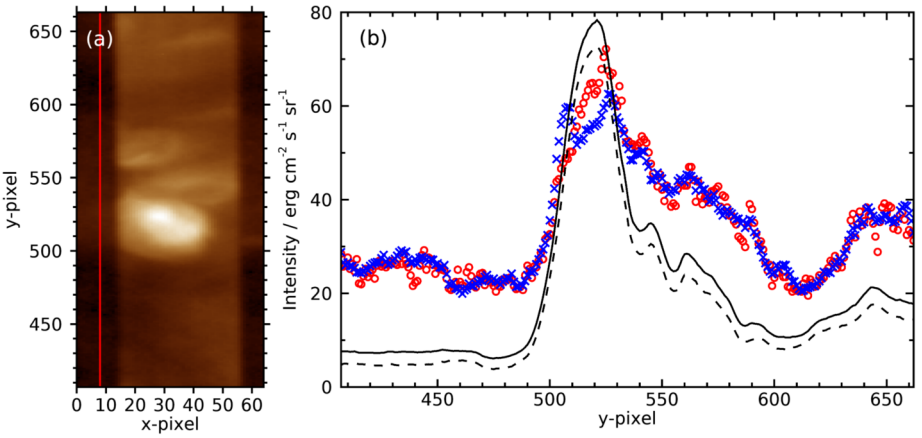

Figure 7 Panel (a) shows the Fe XII λ195.12 slot image from the 16 May 2007 10:46 UT dataset, with a square-root intensity scaling. The *vertical line* shows the location of the pixel that would correspond to the leftmost pixel of a 48-pixel wide window centered on Fe XII λ195.12. The intensity as a function of detector y-pixel position for this pixel is shown as *red circles* on Panel (b). The *blue crosses* show the average intensity for an alternative background prescription (see main text). The *black solid line* shows the Fe XII λ195.12 intensity averaged over the 41-pixel width of the slot and divided by a factor 10 for display purposes. The *black dashed line* shows the λ195.12 intensity variation after background subtraction, also divided by 10.

ii) Estimate the background level along the slot length (Section 5.1).
iii) Subtract the y-dependent background intensity from the slot image intensity.
iv) Divide the subtracted slot image intensity by 1.14.
v) Add an uncertainty of 10% in quadrature to the uncertainty provided by eis_prep, to reflect the uncertainty in the derived slot-to-slit intensity ratios (Section 4.4).

The resulting slot intensities should then be comparable with the slit intensities.

Section 5.2 discusses the procedure to be applied for datasets that have 40-pixel windows for λ195.12.

5.1. Background Subtraction

Section 4.4 provided a method for calculating the background emission using 5-pixel-wide regions located 28 pixels either side of the slot centroid. This was possible because the SYNOP001 study returns the entire EIS wavelength range. Of the 88 slot rasters in the EIS database, 41 use a 40-pixel window for λ195.12, 27 use a 48-pixel window, and the remainder use a window that is 56 pixels or larger. For the latter, the windows are wide enough to give access to background either side of the slot image.

As noted earlier, slot images extend over 46 pixels on the detector, and so there is no background solution for 40-pixel windows (see the following section). For 48-pixel window data, however, it is possible to take advantage of the fact that the slot image is offset to the right side of the wavelength window as highlighted in Section 3.4 and seen visually in Figure 2(a). We can thus use the leftmost column of pixels in the slot image to define the background.

To test this method we selected the SYNOP001 dataset beginning at 10:46 UT on 16 May, which shows a mixture of dark and bright features in the image (Figure 7a). The intensity average over the 41-pixel width of the slit as a function of y-pixel is shown in

Figure 7(b) as a *solid black line*. The *blue crosses* on this panel show the background level derived using the method described in Section 4.4. The *red vertical line* on Figure 7(a) shows the location of the leftmost pixel if a 48-pixel window had been used for the observation. The intensity along this line is shown as *red circles* on Panel (b). Excellent agreement is found with the *blue crosses*, and the standard deviation of the differences between the two background methods is 7.6%. This demonstrates that the 48-pixel window background-subtraction method gives good results.

For this particular dataset the slot image is clearly offset to the right of the wavelength window, and so the method of choosing the leftmost column for the background is successful. Figure 5 shows that the slot image tilts over to the left side of the wavelength window for y-pixels 800 and higher. In addition, there is a 1.5-pixel shift of the slot image during an orbit due to thermal effects that can lead to the slot image being more towards the left of the wavelength window depending on when the exposure is taken. Therefore, our general recommendation for estimating the background from 48-pixel window data is to take the leftmost and rightmost columns of the wavelength window and set the background for a specific row on the detector to be the minimum of these two values.

In summary, for λ195.12 windows of 56 pixels or more it is recommended that the background is calculated by averaging regions either side of the slot image. These regions can either be one or more data columns, or one can select regions that are equidistant from the slot centroid, as done in Section 4.4. For 48-pixel windows, the background can be obtained by taking the minimum value of the left and rightmost columns, as described above. A background estimate is not possible for 40-pixel windows.

5.2. Datasets with 40-Pixel Windows

The previous section noted that 41 of the 88 EIS studies that use the slot use 40-pixel wavelength windows for observing Fe XII λ195.12. Our prescription for computing intensities from the slot data will therefore not work on these datasets since it is not possible to accurately estimate the background intensity level. In Section 4.4 it was noted that the ratio of the slot intensity without background subtraction to the slit intensity becomes constant above slit intensities of 150 erg cm^{-2} s^{-1} sr^{-1}. This suggests the following prescription for 40-pixel data:

i) Calibrate the data to erg cm^{-2} s^{-1} sr^{-1} units.
ii) Divide the slot intensity by a factor 1.27.
iii) Disregard those pixels with intensities less than 150 erg cm^{-2} s^{-1} sr^{-1}.
iv) Add an uncertainty of 10% in quadrature to the uncertainty provided by eis_prep, to reflect the uncertainty in the derived slot-to-slit intensity ratios (Section 4.4).

In particular, this should yield reliable λ195.12 intensities for active regions.

5.3. Extension to Other Emission Lines

Our prescription for correcting the slot intensities applies only to Fe XII λ195.12, and here we discuss whether the method can be extended to other emission lines. It should work for any line that dominates over its immediate neighbors such that the background can be estimated, either on one or both sides of the slot image. Referring to Figure 1, such lines include Fe XI λ180.40, Fe XIII λ202.04, Fe XIII λ203.82, Si X λ258.37, Fe XVI λ262.99, Fe XIV λ274.20, Si VII λ275.36, Mg VIII λ278.40, and Fe XV λ284.16. For each of these it will be necessary to repeat the analysis of Figure 6 to check if the empirical correction factor is

the same and also to determine the cutoff intensity in the case that 40-pixel windows are to be analyzed. As the SYNOP001 study returns the complete EIS wavelength range, then the May 2007 datasets are suitable for each of these additional lines.

6. Summary

The Introduction to this article asked four questions in relation to EIS 40″ slot data, and the answers are listed here.

i) *What is the measured width of the slot?* The width of the slot on the detector shows a small, linear increase from the bottom of the CCD to the top (Figure 4c) with a mean value of 40.949″.
ii) *What is the tilt of the slot on the detector?* The position of the slot image on the detector varies quadratically with detector y-pixel (Figure 4b) with parameters given in Table 2. The image shifts towards shorter wavelengths with increasing y-position, with a total shift of more than 4 pixels from the bottom of the CCD to the top. It was not possible to fully describe the slot tilt for data obtained prior to the EIS grating adjustment of 24 August 2008 and so only a linear fit to the tilt was performed and the gradient is given in Table 4 (31 January 2008 dataset).
iii) *What is the spatial resolution of the slot?* The spatial resolution is measured from the fall-off of intensity at the edge of the slot image, and it varies quadratically with y-position (Figure 4d), with parameters given in Table 2. The best resolution is 2.9″.
iv) *Are the intensities measured with the slot compatible with the narrow slits?* Intensities measured with the slot are around 14% higher than those measured with the 1″ slit, and it is recommended to reduce them by this amount. The background intensity in slot data is significant for intensities typical of quiet-Sun or coronal-hole regions and should be subtracted. A prescription for deriving intensities from the slot data is given in Section 5.

The results presented here should prove valuable to other researchers looking to derive quantitative results from the EIS slot data and exploit the large archive of observations obtained since 2006.

Acknowledgment *Hinode* is a Japanese mission developed and launched by ISAS/JAXA, with NAOJ as domestic partner and NASA and STFC (UK) as international partners. It is operated by these agencies in cooperation with ESA and NSC (Norway). We thank the referee, Dr. J. Dudík, for valuable comments and Dr. E. Landi for planning the observations described in Section 3.2.

Funding P.R. Young acknowledges support from the GSFC Internal Scientist Funding Model competitive work package program and the Heliophysics Guest Investigator program. I. Ugarte-Urra was funded by NASA under a contract to the U.S. Naval Research Laboratory.

Data Availability The level-0 EIS data files used for this work are publicly available from the *Virtual Solar Observatory* (virtualsolar.org) and the *Hinode Science Data Center Europe* (sdc.uio.no). Data derived as part of the analysis for the article are available from the GitHub repository papers/2022_eis_slot.

Declarations

Disclosure of Potential Conflicts of Interest The authors declare that they have no conflicts of interest.

References

Banerjee, D., Teriaca, L., Gupta, G.R., Imada, S., Stenborg, G., Solanki, S.K.: 2009, Propagating waves in polar coronal holes as seen by SUMER & EIS. *Astron. Astrophys.* **499**, L29. DOI. ADS.

Brooks, D.H., Warren, H.P., Williams, D.R., Watanabe, T.: 2009, Hinode/extreme-ultraviolet imaging spectrometer observations of the temperature structure of the quiet corona. *Astrophys. J.* **705**, 1522. DOI. ADS.

Brosius, J.W., Holman, G.D.: 2012, Using SDO's AIA to investigate energy transport from a flare's energy release site to the chromosphere. *Astron. Astrophys.* **540**, A24. DOI. ADS.

Brown, C.M., Feldman, U., Seely, J.F., Korendyke, C.M., Hara, H.: 2008, Wavelengths and intensities of spectral lines in the 171-211 and 245-291 Å ranges from five solar regions recorded by the extreme-ultraviolet imaging spectrometer (EIS) on Hinode. *Astrophys. J. Suppl.* **176**, 511. DOI. ADS.

Chitta, L.P., Peter, H., Young, P.R.: 2021, Extreme-ultraviolet bursts and nanoflares in the quiet-Sun transition region and corona. *Astron. Astrophys.* **647**, A159. DOI. ADS.

Culhane, J.L., Harra, L.K., James, A.M., Al-Janabi, K., Bradley, L.J., Chaudry, R.A., Rees, K., Tandy, J.A., Thomas, P., Whillock, M.C.R., Winter, B., Doschek, G.A., Korendyke, C.M., Brown, C.M., Myers, S., Mariska, J., Seely, J., Lang, J., Kent, B.J., Shaughnessy, B.M., Young, P.R., Simnett, G.M., Castelli, C.M., Mahmoud, S., Mapson-Menard, H., Probyn, B.J., Thomas, R.J., Davila, J., Dere, K., Windt, D., Shea, J., Hagood, R., Moye, R., Hara, H., Watanabe, T., Matsuzaki, K., Kosugi, T., Hansteen, V., Wikstol, Ø.: 2007a, The EUV imaging spectrometer for Hinode. *Solar Phys.* **243**, 19. DOI. ADS.

Culhane, L., Harra, L.K., Baker, D., van Driel-Gesztelyi, L., Sun, J., Doschek, G.A., Brooks, D.H., Lundquist, L.L., Kamio, S., Young, P.R., Hansteen, V.H.: 2007b, Hinode EUV study of jets in the Sun's South polar corona. *Publ. Astron. Soc. Japan* **59**, S751. DOI. ADS.

Del Zanna, G.: 2013, A revised radiometric calibration for the Hinode/EIS instrument. *Astron. Astrophys.* **555**, A47. DOI. ADS.

Del Zanna, G., Dere, K.P., Young, P.R., Landi, E.: 2021, CHIANTI—an atomic database for emission lines. XVI. Version 10, further extensions. *Astrophys. J.* **909**, 38. DOI. ADS.

Delaboudinière, J.-P., Artzner, G.E., Brunaud, J., Gabriel, A.H., Hochedez, J.F., Millier, F., Song, X.Y., Au, B., Dere, K.P., Howard, R.A., Kreplin, R., Michels, D.J., Moses, J.D., Defise, J.M., Jamar, C., Rochus, P., Chauvineau, J.P., Marioge, J.P., Catura, R.C., Lemen, J.R., Shing, L., Stern, R.A., Gurman, J.B., Neupert, W.M., Maucherat, A., Clette, F., Cugnon, P., van Dessel, E.L.: 1995, EIT: extreme-ultraviolet imaging telescope for the SOHO mission. *Solar Phys.* **162**, 291. DOI. ADS.

Harra, L.K., Hara, H., Doschek, G.A., Matthews, S., Warren, H., Culhane, J.L., Woods, M.M.: 2017, Measuring velocities in the early stage of an eruption: using "overlappogram" data from Hinode EIS. *Astrophys. J.* **842**, 58. DOI. ADS.

Harra, L., Matthews, S., Long, D., Hasegawa, T., Lee, K.-S., Reeves, K.K., Shimizu, T., Hara, H., Woods, M.: 2020, Locating hot plasma in small flares using spectroscopic overlappogram data from the Hinode EUV imaging spectrometer. *Solar Phys.* **295**, 34. DOI. ADS.

Harrison, R.A., Sawyer, E.C., Carter, M.K., Cruise, A.M., Cutler, R.M., Fludra, A., Hayes, R.W., Kent, B.J., Lang, J., Parker, D.J., Payne, J., Pike, C.D., Peskett, S.C., Richards, A.G., Gulhane, J.L., Norman, K., Breeveld, A.A., Breeveld, E.R., Al Janabi, K.F., McCalden, A.J., Parkinson, J.H., Self, D.G., Thomas, P.D., Poland, A.I., Thomas, R.J., Thompson, W.T., Kjeldseth-Moe, O., Brekke, P., Karud, J., Maltby, P., Aschenbach, B., Bräuninger, H., Kühne, M., Hollandt, J., Siegmund, O.H.W., Huber, M.C.E., Gabriel, A.H., Mason, H.E., Bromage, B.J.I.: 1995, The coronal diagnostic spectrometer for the solar and heliospheric observatory. *Solar Phys.* **162**, 233. DOI. ADS.

Innes, D.E., Attie, R., Hara, H., Madjarska, M.S.: 2008, EIS/Hinode observations of Doppler flow seen through the 40-arcsec wide-slit. *Solar Phys.* **252**, 283. DOI. ADS.

Kamio, S., Hara, H., Watanabe, T., Fredvik, T., Hansteen, V.H.: 2010, Modeling of EIS spectrum drift from instrumental temperatures. *Solar Phys.* **266**, 209. DOI. ADS.

Kennedy, L., Young, P.R.: 2022, Eis software note no. 6: warm and hot pixels on the eis ccds. DOI.

Kohl, J.L., Esser, R., Gardner, L.D., Habbal, S., Daigneau, P.S., Dennis, E.F., Nystrom, G.U., Panasyuk, A., Raymond, J.C., Smith, P.L., Strachan, L., van Ballegooijen, A.A., Noci, G., Fineschi, S., Romoli, M., Ciaravella, A., Modigliani, A., Huber, M.C.E., Antonucci, E., Benna, C., Giordano, S., Tondello, G., Nicolosi, P., Naletto, G., Pernechele, C., Spadaro, D., Poletto, G., Livi, S., von der Lühe, O., Geiss, J., Timothy, J.G., Gloeckler, G., Allegra, A., Basile, G., Brusa, R., Wood, B., Siegmund, O.H.W., Fowler, W., Fisher, R., Jhabvala, M.: 1995, The ultraviolet coronagraph spectrometer for the solar and heliospheric observatory. *Solar Phys.* **162**, 313. DOI. ADS.

Kontogiannis, I., Gontikakis, C., Tsiropoula, G., Tziotziou, K.: 2018, Probing the quiet solar atmosphere from the photosphere to the corona. *Solar Phys.* **293**, 56. DOI. ADS.

Korendyke, C.M., Brown, C.M., Thomas, R.J., Keyser, C., Davila, J., Hagood, R., Hara, H., Heidemann, K., James, A.M., Lang, J., Mariska, J.T., Moser, J., Moye, R., Myers, S., Probyn, B.J., Seely, J.F., Shea, J., Shepler, E., Tandy, J.: 2006, Optics and mechanisms for the Extreme-Ultraviolet Imaging Spectrometer on the Solar-B satellite. *Appl. Opt.* **45**, 8674. DOI. ADS.

Lang, J., Kent, B.J., Paustian, W., Brown, C.M., Keyser, C., Anderson, M.R., Case, G.C.R., Chaudry, R.A., James, A.M., Korendyke, C.M., Pike, C.D., Probyn, B.J., Rippington, D.J., Seely, J.F., Tandy, J.A., Whillock, M.C.R.: 2006, Laboratory calibration of the Extreme-Ultraviolet Imaging Spectrometer for the Solar-B satellite. *Appl. Opt.* **45**, 8689. DOI. ADS.

Lemen, J.R., Title, A.M., Akin, D.J., Boerner, P.F., Chou, C., Drake, J.F., Duncan, D.W., Edwards, C.G., Friedlaender, F.M., Heyman, G.F., Hurlburt, N.E., Katz, N.L., Kushner, G.D., Levay, M., Lindgren, R.W., Mathur, D.P., McFeaters, E.L., Mitchell, S., Rehse, R.A., Schrijver, C.J., Springer, L.A., Stern, R.A., Tarbell, T.D., Wuelser, J.-P., Wolfson, C.J., Yanari, C., Bookbinder, J.A., Cheimets, P.N., Caldwell, D., Deluca, E.E., Gates, R., Golub, L., Park, S., Podgorski, W.A., Bush, R.I., Scherrer, P.H., Gummin, M.A., Smith, P., Auker, G., Jerram, P., Pool, P., Soufli, R., Windt, D.L., Beardsley, S., Clapp, M., Lang, J., Waltham, N.: 2012, The Atmospheric Imaging Assembly (AIA) on the Solar Dynamics Observatory (SDO). *Solar Phys.* **275**, 17. DOI. ADS.

Markwardt, C.B.: 2009, Non-linear least-squares fitting in IDL with MPFIT. In: Bohlender, D.A., Durand, D., Dowler, P. (eds.) *Astronomical Data Analysis Software and Systems XVIII*, *Astronomical Society of the Pacific Conference Series* **411**, 251. ADS.

O'Shea, E., Doyle, J.G.: 2009, On oscillations found in an active region with EIS on Hinode. *Astron. Astrophys.* **494**, 355. DOI. ADS.

Peter, H.: 2010, Asymmetries of solar coronal extreme ultraviolet emission lines. *Astron. Astrophys.* **521**, A51. DOI. ADS.

Srivastava, A.K., Dwivedi, B.N.: 2010a, Observations from Hinode/EIS of intensity oscillations above a bright point: signature of the leakage of acoustic oscillations in the inner corona. *Mon. Not. Roy. Astron. Soc.* **405**, 2317. DOI. ADS.

Srivastava, A.K., Dwivedi, B.N.: 2010b, Signature of slow acoustic oscillations in a non-flaring loop observed by EIS/Hinode. *New Astron.* **15**, 8. DOI. ADS.

Ugarte-Urra, I.: 2016 EIS Software Note No. 8. EIS Point Spread Function. Technical report. https://sohoftp.nascom.nasa.gov/solarsoft/hinode/eis/doc/eis_notes/08_COMA/eis_swnote_08.pdf.

Ugarte-Urra, I., Warren, H.P.: 2011, Temporal variability of active region outflows. *Astrophys. J.* **730**, 37. DOI. ADS.

Ugarte-Urra, I., Warren, H.P., Brooks, D.H.: 2009, Active region transition region loop populations and their relationship to the corona. *Astrophys. J.* **695**, 642. DOI. ADS.

Warren, H.P., Ugarte-Urra, I., Landi, E.: 2014, The absolute calibration of the EUV imaging spectrometer on Hinode. *Astrophys. J. Suppl.* **213**, 11. DOI. ADS.

Warren, H.P., Ugarte-Urra, I., Young, P.R., Stenborg, G.: 2011, The temperature dependence of solar active region outflows. *Astrophys. J.* **727**, 58. DOI. ADS.

Wilhelm, K., Curdt, W., Marsch, E., Schühle, U., Lemaire, P., Gabriel, A., Vial, J.-C., Grewing, M., Huber, M.C.E., Jordan, S.D., Poland, A.I., Thomas, R.J., Kühne, M., Timothy, J.G., Hassler, D.M., Siegmund, O.H.W.: 1995, SUMER - solar ultraviolet measurements of emitted radiation. *Solar Phys.* **162**, 189. DOI. ADS.

Winebarger, A.R., Weber, M., Bethge, C., Downs, C., Golub, L., DeLuca, E., Savage, S., del Zanna, G., Samra, J., Madsen, C., Ashraf, A., Carter, C.: 2019, Unfolding overlapped slitless imaging spectrometer data for extended sources. *Astrophys. J.* **882**, 12. DOI. ADS.

Woods, T.N., Eparvier, F.G., Hock, R., Jones, A.R., Woodraska, D., Judge, D., Didkovsky, L., Lean, J., Mariska, J., Warren, H., McMullin, D., Chamberlin, P., Berthiaume, G., Bailey, S., Fuller-Rowell, T., Sojka, J., Tobiska, W.K., Viereck, R.: 2012, Extreme ultraviolet variability experiment (EVE) on the solar dynamics observatory (SDO): overview of science objectives, instrument design, data products, and model developments. *Solar Phys.* **275**, 115. DOI. ADS.

Young, P.R.: 2021, Future prospects for solar EUV and soft X-ray solar spectroscopy missions. *Front. Astron. Space Sci.* **8**, 50. DOI. ADS.

Young, P.R.: 2022a, Calibrating EIS data: the EIS_PREP routine. Technical report. DOI.
Young, P.R.: 2022b, EIS_AUTO_FIT and SPEC_GAUSS_EIS: Gaussian fitting routines for the Hinode/EIS mission. Technical report. DOI.
Young, P.R., Watanabe, T., Hara, H., Mariska, J.T.: 2009, High-precision density measurements in the solar corona. I. Analysis methods and results for Fe XII and Fe XIII. *Astron. Astrophys.* **495**, 587. DOI. ADS.
Young, P.R., Dere, K.P., Landi, E., Del Zanna, G., Mason, H.E.: 2016, The CHIANTI atomic database. *J. Phys. B, At. Mol. Phys.* **49**, 074009. DOI. ADS.